

## Satellite and Radar Remote Sensing of Southern Plains Grass Fires: A Case Study

THOMAS A. JONES

*Earth System Science Center, University of Alabama in Huntsville, Huntsville, Alabama*

SUNDAR A. CHRISTOPHER

*Earth System Science Center, and Department of Atmospheric Science, University of Alabama in Huntsville, Huntsville, Alabama*

(Manuscript received 14 January 2010, in final form 27 April 2010)

### ABSTRACT

Many large grass fires occurred in north Texas and southern Oklahoma on 9 April 2009, destroying hundreds of homes and businesses and burning thousands of acres of grasslands, producing large smoke and debris plumes that were visible from various remote sensing platforms. At the same time, strong westerly winds were transporting large amounts of dust into the region, mixing with the smoke and debris already being generated. This research uses surface- and satellite-based remote sensing observations of this event to assess the locations of fires and the spatial distribution of smoke and dust aerosols. The authors present a unique perspective by analyzing radar observations of fire debris in conjunction with the satellite analysis of submicrometer smoke aerosol particles. Satellite data clearly show the location of the individual fires and the downwind smoke plumes as well as the large dust storm present over the region. In particular, Moderate Resolution Imaging Spectroradiometer (MODIS) aerosol optical thickness at  $0.55\ \mu\text{m}$  within the dust plume was around 0.5, and it increased to greater than 1.0 when combined with smoke. Using the difference in 11- versus 12- $\mu\text{m}$  brightness temperature data combined with surface observations, the large extent of the dust plume was evident through much of north-central Texas, where visibilities were low and the 11–12- $\mu\text{m}$  brightness temperature difference was negative. Conversely, smoke plumes were characterized by higher reflectance at  $0.6\ \mu\text{m}$  (visible wavelength). Cross sections of radar data through the several smoke and debris plumes indicated the burnt debris reached up to 5 km into the atmosphere. Plume height output from modified severe storm algorithms produced similar values. Since smoke aerosols are smaller and lighter when compared with the debris, they were likely being transported even higher into the atmosphere. These results show that the combination of satellite and radar data offers a unique perspective on observing the characteristics and evolution of smoke and debris plume emanating from grass fire events.

### 1. Introduction

A grass fire outbreak occurred throughout north Texas and southern Oklahoma on 9 April 2009 and destroyed hundreds of homes and businesses while consuming thousands of acres of grasslands and causing millions of dollars in damages and destruction of livestock (*Times-Record News*, 10 April 2009). This event followed a similar grass fire outbreak that occurred over the same area on 27 December 2005, which also destroyed over 1000 homes and businesses, killed 19 people, and

resulted in hundreds of millions of dollars in damages (Weaver 2006). Prior to both events, severe drought conditions existed throughout this region according to the National Drought Mitigation Center (NDMC; Wilhite et al. 1996), resulting in large areas of dead, dry grass and brush that served as fuel for the ensuing fires. Several important factors combined to produce these widespread fire outbreaks. In 2005, a cold front and associated dryline were moving eastward through north Texas, producing winds in excess of  $15\ \text{m s}^{-1}$  and a relative humidity less than 15% (Weaver 2006). On 9 April 2009, a deepening low pressure system was centered in central Oklahoma moving northeast, with a trailing dryline located near the Interstate (highway)-35 corridor between Oklahoma City, Oklahoma, and Dallas, Texas. Strong winds picked up dust from western

---

*Corresponding author address:* Thomas Jones, Earth System Science Center, University of Alabama in Huntsville, 320 Sparkman Drive, NSSTC, Huntsville, AL 35805.  
E-mail: tjones@nsstc.uah.edu

TABLE 1. Brief summary of individual sensor characteristics and important products used in this research.

Sensor	Resolution	Time	Comments
MODIS	1–10 km	Twice daily	Multispectral dust, smoke, and cloud properties
GOES	1–4 km	≤30 min	Visible and IR dust, smoke, and cloud properties
WSR-88D	1 km	≤10 min	3D debris properties; velocity information
Surface	Point	≤30 min	Atmospheric conditions and visibility

Texas, reducing visibility and air quality behind the dryline. Furthermore, these winds caused damage to power lines, sparking fires that, once started, spread very rapidly. Other fires were started by accident and/or embers left over from previous grass fires that had occurred during the prior week. The resulting fires persisted well into the evening hours of 9 April and were not completely under control until the next day, burning over 150 000 acres across Texas and Oklahoma (see Situation Reports online at <http://www.txdps.state.tx.us/dem>; <http://agblog.ok.gov/>).

Of the many fires that occurred on this day, several produced large smoke and debris plumes that were visible from various satellite- and surface-based remote sensing platforms. There is a distinct difference between a smoke and debris plume, even though they are often collocated (Jones and Christopher 2009). A smoke plume is defined as being composed primarily of smoke aerosol particles, while a debris plume corresponds to where partially burnt debris such as grass blades and pine needles are lofted into the atmosphere. We analyze data from the Moderate Resolution Imaging Spectroradiometer (MODIS) and Geostationary Operational Environmental Satellite (*GOES-12*)-based sensors as well as surface-based Weather Surveillance Radar-1988 Doppler (WSR-88D). A nontechnical analysis of this event has been presented by the authors under the “Map Room” section of the *Bulletin of the American Meteorological Society* (Jones and Christopher 2010). In this paper, we more closely examine the unique abilities of each sensor to sample various characteristics of smoke and debris plumes and note that a combination of these data permit a greater understanding of these plumes and their evolution than was previously possible. These sensors can also provide the spatial and vertical distributions of debris and/or aerosols and their properties that are critical for air quality modeling simulations and aerosol radiative effects (Christopher et al. 2009). Relevant observations and available resolutions of each sensor used by this study are summarized in Table 1.

Several previous studies have examined wildfire characteristics from controlled burns using in situ and remote sensing measurements (e.g., Cheney and Gould 1995; Clements et al. 2007). The properties of these fires and the corresponding smoke and debris plumes are a

function of the material being burned. Depending on location, wildfires may burn forests, brush, grasslands, and even man-made structures over either flat or mountainous terrain. Forests fires, also labeled crown fires since they burn suspended material at the canopy level, are generally the strongest in that they have the largest observed sensible heat fluxes and updraft velocities. Updrafts of up to  $20 \text{ m s}^{-1}$  have been measured in these environments (Banta et al. 1992; Clark et al. 1999; Coen et al. 2004). Grass and brush fires burn material nearer the surface, producing smaller heat fluxes and weaker updrafts, generally between 5 and  $10 \text{ m s}^{-1}$  (Clements et al. 2007). Still, an updraft of  $10 \text{ m s}^{-1}$  is capable of lofting debris and ash whose sizes can range up to 1 cm in diameter into the atmosphere. The height to which this debris is lofted is a function of the weight and size of the debris as well as the updraft velocity. Thus, fires that have larger heat fluxes and updraft velocities should inject a larger amount of debris into the atmosphere compared to a smaller, weaker fire. As the spatial coverage and/or heat flux associated with a fire increases, a corresponding increase should be observed in radar reflectivity.

In addition to the debris particles, these fires also loft large amounts of smaller smoke aerosol particles into the atmosphere. While not generally detectable from radars, they are detectable from satellite remote sensors such as MODIS and the GOES imager that measure visible radiation. Smoke aerosols are highly reflective in the visible portion of the electromagnetic spectrum, making them appear brighter than the surface background. Satellite-based remote sensing has utilized visible light observations to sample the size, particle size concentration, and evolution of smoke plume emanating from wildfires. However, these sensors generally do not provide much information concerning vertical distribution of smoke aerosols on a timely basis, something a radar can easily do for debris (Table 1). The goal of this research is to combine radar and satellite observations to provide a link between smoke and debris plume observations as well as compare the advantages and disadvantages of each sensor. By bridging the gap between debris and smoke aerosol observations, we believe that a greater understanding of wildfire impacts can be gained, possibly

leading to the creation of future tools to predict these impacts and how they may affect human activities.

## 2. Data and methods

The MODIS on the *Terra* and *Aqua* satellites measures reflected and emitted radiation from the earth-atmosphere system in 36 spectral channels between 0.405 and 14.385  $\mu\text{m}$ , with a swath width of 2330 km providing a near-daily global coverage. Data are collected at spatial resolutions of 250 m, 500 m, and 1 km depending on wavelength. We use 1-km visible reflectance and brightness temperature data to determine the locations and spectral characteristics of the dust and smoke present during this event. The Collection 5 level 2 (L2) aerosol product is generated at a 10 km<sup>2</sup> resolution using a set of 20  $\times$  20 (400) 500-m pixels. This product represents a total columnar value of aerosol extinction and allows for global mapping of particulate matter from space over cloud-free regions (Chu et al. 2002). The aerosol retrieval algorithm over land uses reflectance from three channels (0.47, 0.67, 2.13  $\mu\text{m}$ ) and reports the aerosol optical thickness (AOT) at 0.55  $\mu\text{m}$  (Remer et al. 2005; Levy et al. 2007). The retrieval algorithm works by matching the observed reflectance values to expected values based on radiative transfer model generated lookup tables for various aerosol types. Once a best-fit match is made, the AOT value can be retrieved. An AOT closer to zero indicates a pristine, clear-sky atmosphere with increasing AOT values corresponding to an increase in tropospheric aerosol content. AOT values near 1.0 indicate very heavy aerosol concentrations. The algorithm does have some difficulties and may report anomalous values in the vicinity of clouds and over bright surfaces (Levy et al. 2007). Infrared products are also useful in determining aerosol characteristics. One such product is the difference between 11- and 12- $\mu\text{m}$  brightness temperatures. Infrared radiation at these wavelengths can be affected through absorption by dust aerosols, while smaller, submicrometer smoke aerosols are more transparent in the IR. Dust aerosol particles have a spectral dependence in the IR whereby the difference between 11- and 12- $\mu\text{m}$  brightness temperatures ( $T_{b11} - T_{b12}$ ) is negative since these aerosols are more absorptive at 12  $\mu\text{m}$  (Sokolik and Toon 1999). For illustration purposes, the “MYD14” MODIS fire detection product was obtained for the same time period from the *Aqua* satellite. Fires are identified using a contextual algorithm for fire detection and report the location and temperatures of various “hot spots” at the time of the satellite overpass (Giglio et al. 2003; Justice et al. 2002; Prados et al. 2007).

The imager on the *GOES-12* satellite also provides information on reflected and emitted radiation in the

visible and infrared spectrum. Visible (1 km) and infrared (4 km) data are available at least every 30 min, making possible a study of the time evolution of dust and smoke not possible with the MODIS data. The GOES Wild Fire Automated Biomass Burning Algorithm (ABBA) also provides near-real-time locations of fires and hot spots throughout the Western Hemisphere at 30-min intervals using data from *GOES-12* (Prins and Menzel 1994). These data are used in combination with the radar data (described below) to create a time series of debris plume heights for individual fires.

Another important method to sample the evolution of these fires is the use of ground-based radars, namely the WSR-88Ds present throughout the United States. The WSR-88D network consists of approximately 150 operational radars operated by the National Oceanic and Atmospheric Administration (NOAA) and National Weather Service (NWS). The WSR-88D is an active S-band (10 cm) precipitation radar, with an azimuthal resolution of 1° and a range bin of 1 km providing a 3D data volume every 5–6 min (Crum and Alberty 1993). The fires occurred within range of four WSR-88Ds (KTLX, KFDR, KDYX, and KFWS located near Oklahoma City and Frederick, Oklahoma; and Abilene and Dallas, Texas respectively) providing excellent spatial sampling over a large area. Both KFWS and KTLX operated in precipitation mode throughout the event with KFDR switching over after 2200 UTC. Conversely, KDYX operated in clear-air mode throughout the event. Note that the maximum elevation scan used by the clear-air mode is only 3.5°; thus, the vertical extent of debris plumes may be underestimated during this scanning strategy (Crum and Alberty 1993).

It is important to recall that these radars are generally not sensitive to the smoke or dust aerosols themselves ( $D \sim 1 \mu\text{m}$ ) but to the much larger burnt grass and other debris ( $D > 100 \mu\text{m}$ ) lofted into the atmosphere by the buoyant updrafts produced from the heat of the fires (Rothermel 1991; Rogers and Brown 1997; Jones and Christopher 2009; Jones et al. 2009). The advantages of using precipitation radars during fire events are many. First, these radars provide high spatial resolution data ( $\sim 1$  km or less) in both the horizontal and vertical planes at a temporal resolution of 10 min or less. Moreover, these observations are available within minutes of real time, unlike some other remote sensing products. Relative to most satellite observations, the radar data represent either improved spatial resolution or, especially, improved temporal resolution. Currently, very few objective methods for using radar data in wildfire research exist, but this research along with other efforts is increasingly exploring this possibility (Melnikov et al. 2008; Jones et al. 2009; Jones and Christopher 2009).

To objectively determine injection height from WSR-88D data, we use a modified version of the Storm Cell Identification and Tracking (SCIT) algorithm, which was designed to detect and report spatial and temporal characteristics of individual storm cells (Johnson et al. 1998). Often, large debris plumes have high radar reflectivity values near the source fire where the debris concentration is greatest, with reflectivity decreasing downwind as the larger debris particles fall out of the atmosphere. Thunderstorms have a similar appearance with the greatest reflectivity near the core of the storm associated with heavy rain and/or hail with lower reflectivity downwind corresponding to the storm anvil. SCIT operates by analyzing 2D slices of a reflectivity field at a particular time and determining regions of contiguous reflectivity returns exceeding a certain threshold (30 dBZ operationally). This process is repeated for all levels (or elevation scans when only a single radar is used) producing a database of 2D reflectivity features. SCIT combines these 2D features into 3D storm cell detections by collocating individual 2D features from different elevations. SCIT returns many storm parameters including volume coverage, base and maximum heights, height and value of maximum reflectivity, and whether it is collocated with any rotational velocity features. The maximum height parameter, or storm top, defines the highest level at which reflectivity greater than a predefined threshold exists, which for this research is defined as injection height.

Fortunately, lofted debris often exhibit similar characteristics to those observed in supercell thunderstorms, just on a smaller and less intense scale. To detect these plumes, we modified SCIT to detect “storms” using reflectivity thresholds as low as 10 dBZ compared to the 30-dBZ value used operationally. To remove possible precipitation-based storm cell detections, each detection was compared with GOES ABBA fire product, and storm cells not within  $\pm 30$  min and  $\pm 30$  km of a GOES fire pixel are filtered out. In the future, it will be possible to use WSR-88Ds upgraded with dual-polarimetric capabilities to distinguish between precipitation and debris. Debris lofted into the air from fires are generally nonspherical in nature and have much different scattering properties than do raindrops allowing for a clear distinction between the two to be made (Melnikov et al. 2008; Jones et al. 2009).

Atmospheric conditions are obtained from hourly observations by the network of Automated Surface Observing Systems (ASOS) present throughout the United States. Data available from these instruments include temperature, humidity, pressure, wind speed (sustained and gusts) and direction, and finally visibility. Humidity and wind speed data were used to assess the location of the dryline and intensity of the westerly winds behind it.

Visibility data were compared with the satellite observations to validate the location, size, and progression of the dust and smoke plumes during this event. Aerosol and air quality data from other surface-based instruments such as the Aerosol Robotic Network (AERONET) and Improvement of Microphysical Parameterization through Observational Verification Experiment (IMPROVE) were not available at the times and/or locations necessary to sample the dust and smoke aerosols. Only a single instrument of each type exists within the domain of study (AERONET near Oklahoma City and IMPROVE near Frederick) and in both cases measurements were either not made or not available for 9 April 2009 (Fig. 1a). Given the poor sampling of surface-based sensors in this region, it is clear that remote sensing is better suited to assess the characteristics of the dust and smoke plumes associated with this event.

### 3. Atmospheric conditions

According to the NDMC, severe drought conditions existed over portions of north Texas and southern Oklahoma during the month leading up to these fires. The persistent dry conditions delayed the onset of spring vegetation leaving dried-out winter growth in place, which acted as fuel for the ensuing fires. These fuels primarily included dry grass and brush with widespread structure fires also evident at times. The catalyst for the 9 April fires was a deepening low pressure system in northeastern Oklahoma associated with a dryline that became better defined as the afternoon progressed. The eastward progression of the dryline is evident in both GOES and WSR-88D data as a line of thin clouds and weak radar reflectivity ( $\sim 10$  dBZ) traveling eastward as a function of time (Figs. 2 and 3). Westerly winds behind the dryline quickly increased to in excess of  $15 \text{ m s}^{-1}$  with a maximum gust of  $34 \text{ m s}^{-1}$  ( $76 \text{ mi h}^{-1}$ ) recorded southeast of Frederick, Oklahoma, at 1925 UTC (Norman, Oklahoma; National Weather Service 2009). Winds remained strong throughout the afternoon and did not decrease substantially until well after 0000 UTC 10 April (Fig. 4a). Behind the dryline was a large area of warm and very low humidity air ( $\text{RH} < 20\%$ ) (Fig. 4b). Surface observations between 1600 UTC 9 April and 0400 UTC 10 April show dry, windy conditions present throughout this region, especially for sites located in Texas (Figs. 4a,b). The dryline passed Gainesville, Texas (KGLE), and Ardmore, Oklahoma (KADM), at 2000 and 2200 UTC, respectively, corresponding to a large decrease in relative humidity at these stations (Fig. 4b). Also of note are the low visibilities ( $< 6$  km) caused by the extreme amounts of dust in the atmosphere. In particular, visibility at both Abilene, Texas (KABI),

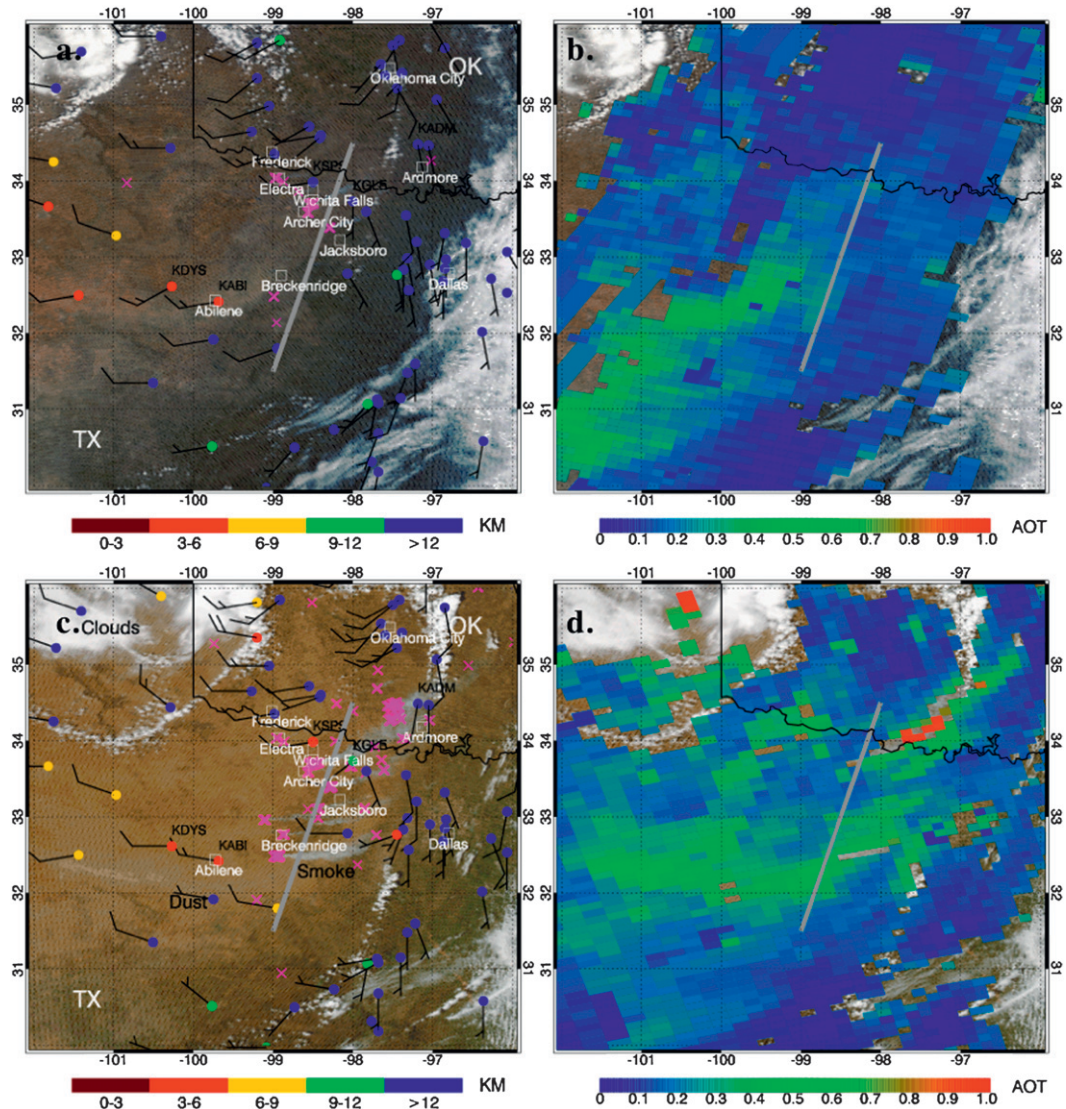


FIG. 1. (a) *Terra* and (c) *Aqua* MODIS level 1B true color images over north Texas and southern Oklahoma at 1630 and 1930 UTC 9 Apr 2009 creating using 0.47-, 0.55-, and 0.67- $\mu\text{m}$  visible reflectance. Smoke plumes are evident in the *Aqua* image as grayish white regions aligned in a north–south manner near the center of the image. MOD14 hot spots at these times are overlaid, indicating the locations of the individual fires. ASOS surface stations are also plotted and color coded to represent visibility at each site, with blue indicating >12 km visibility and red indicating <6 km visibility. (b) *Terra* and (d) *Aqua* MODIS level 2 AOT at 0.55- $\mu\text{m}$  data at these times. Note the high AOT values associated with the large dust plume and how it increases when mixed with smoke from the fires. The gray line corresponds to a cross section of satellite and radar data shown in Figs. 5 and 6.

and Dyess Air Force Base (KDYS) was often below 6 km between 1700 and 2200 UTC (Fig. 4b). Reduction in visibility due to smoke plumes was actually less than that observed for dust. Stations ahead of the smoke plumes include KGLE and KADM. Visibility at both locations decreased to around 8 km after 2200 UTC. If not for the grass fires, the impact of the dust storm would have been considered a significant event by itself.

Given the strong winds and abnormally dry conditions, the environment was very favorable to the propagation of grass fires over a large region. These conditions were well forecasted by the NWS, which issued fire weather watches for the region 48 h in advance and a red flag warning early in the morning of 9 April. As the outbreak progressed, the Norman NWS Office issued multiple nowcasts and fire warning products stating the locations and predicted near-term evolution of individual

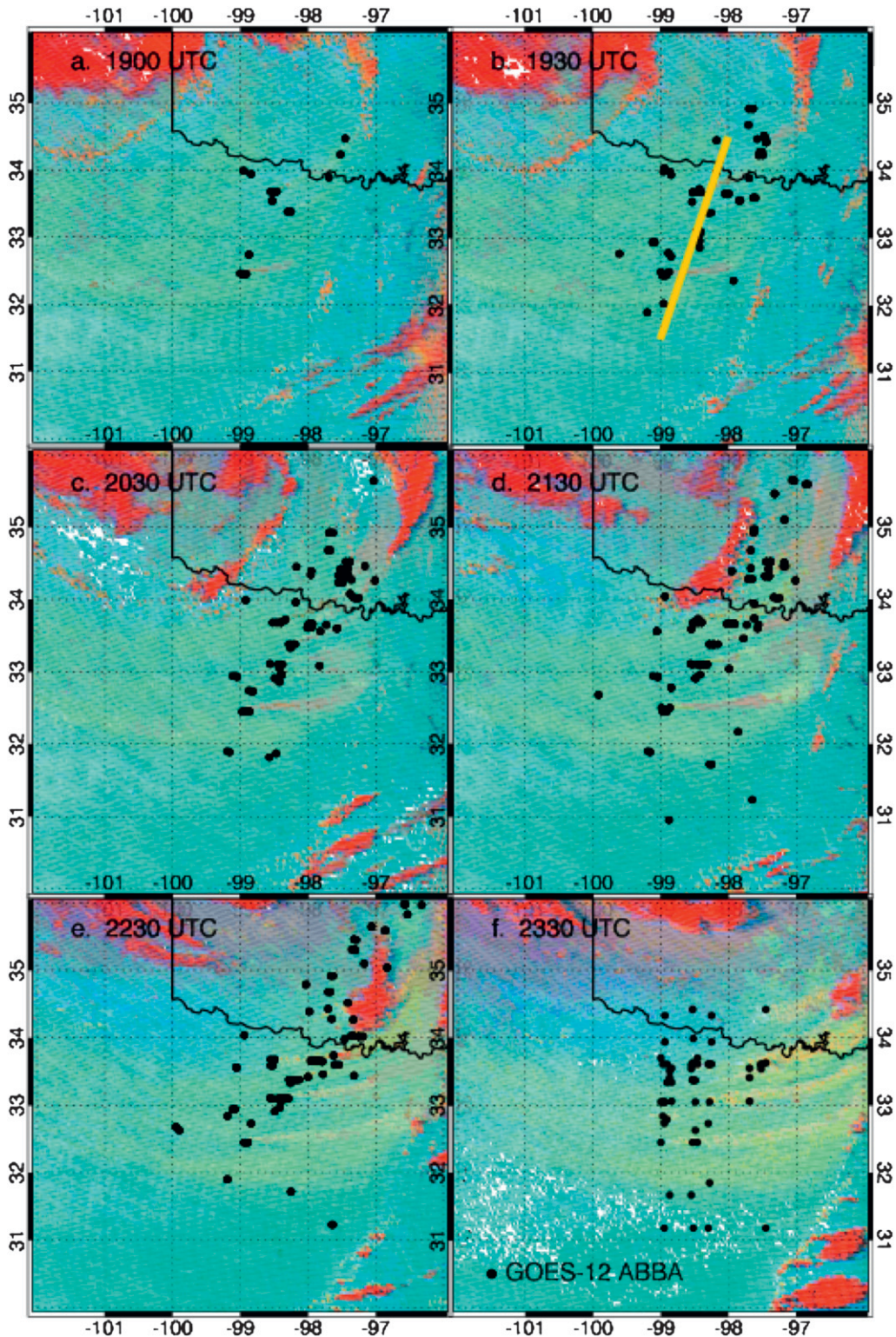


FIG. 2. GOES false color images (red = visible, green =  $3.9 \mu\text{m}$ , blue =  $10.7 - 13.3 \mu\text{m}$  difference) from (a) 1900, (b) 1930, (c) 2030, (d) 2130, (e) 2230, and (f) 2330 UTC. Bright red areas indicate regions of clouds, with light blue indicating clear-sky areas. Dust is visible as yellow green color, which becomes most apparent by 2330 UTC. The orange line in (b) is at the same location as that in Fig. 1, corresponding to the cross section of satellite and radar data shown in Figs. 5 and 6. Black dots indicate locations of individual *GOES-12* ABBA fire detections within  $\pm 30$  min of each panel time.

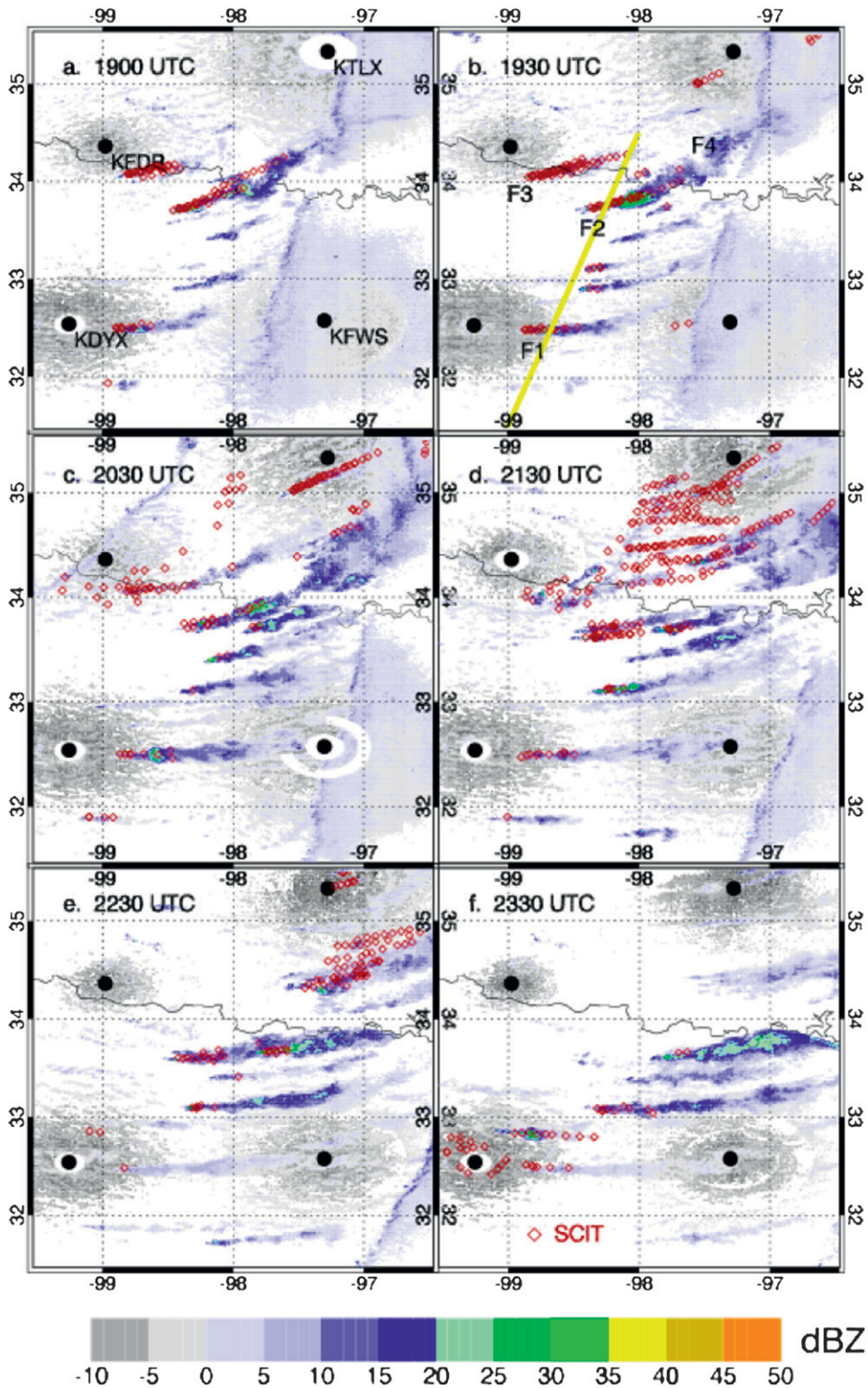


FIG. 3. WSR-88D reflectivity data (dBZ) (from KDYX, KFDR, KFWS, and KTLX) for (a)–(f) 1900–2330 UTC 9 Apr corresponding to time series of GOES data in Fig. 2. Large black circles indicating the location of each radar are labeled in (a). Approximate height of radar data is 1 km, with a horizontal resolution of 1 km. The debris plumes are clearly evident as areas of enhanced reflectivity, with some having plumes appearing to be greater than 100 km in length. The dryline and its movement eastward are also detectable near KFWS and KTLX. Overlaid on each panel as red diamonds are SCIT “storm cell” detections for each debris plume within  $\pm 30$  min of each panel time.

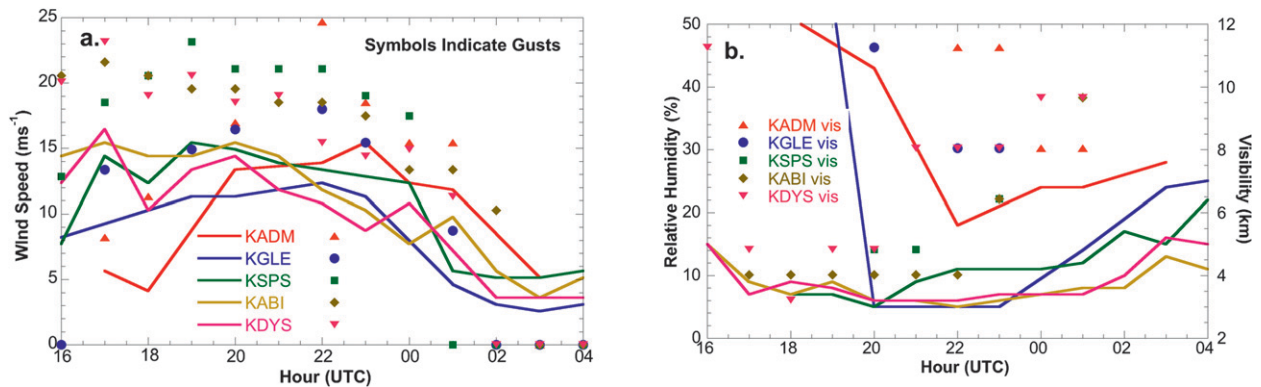


FIG. 4. Time series of ASOS (a) wind speeds (lines) and gusts (symbols) and (b) relative humidity (lines) and surface visibility (symbols) between 1600 UTC 9 Apr and 0400 UTC 10 Apr for five sites in north Texas and southern Oklahoma.

fires using data from various surface and remote sensing data sources. The number of fires was such that warnings were being issued in a manner similar to that used during a large severe weather outbreak. However, during the latter case, more automated tools exist to examine the raw data directing where the forecaster should focus their resources. These tools do not yet exist for short-term fire impact forecasts and part of this research is to assess how these data can be used in the creation of such tools.

#### 4. Remote sensing overview

##### a. Satellite data

During the *Terra* overpass at 1630 UTC (1130 local time), the dust plume was evident in west-central Texas with corresponding AOT between 0.2 and 0.5 (Figs. 1a,b). The fires have yet to become strong and no large smoke plumes were yet visible within the MODIS imagery. By the time of the *Aqua* MODIS overpass at 1930 UTC (1430 local time), the location of the individual fires and the downwind smoke plumes were much more evident (Fig. 1c). Smoke plumes existed over 100 km downwind of the strongest fires whose approximate origin is given by the MODIS (MYD14) hot spot detections within Fig. 1c. The greatest concentration of hot spots occurred in south-central Oklahoma and north Texas. Other important features visible include a line of clouds oriented north-south east of the fires associated with the location of the dryline. Another line of clouds was present in western Oklahoma associated with a cold front moving through behind the dryline. The maximum number of fires occurred in this window after the passage of the dryline, but before the passage of the cold front, behind which winds were somewhat weaker.

MODIS AOT from *Aqua* within the dust plume was around 0.5 increasing to greater than 1.0 when combined

with smoke from the various fires (Fig. 1d). The greatest AOT values were observed in southern Oklahoma near Ardmore corresponding to several grass fires, which are clearly observable in the raw imagery and hot spot detections shown in Fig. 1c. In northwestern Oklahoma behind the cold front, AOT was less than 0.15 during the *Terra* overpass as dust was not being transported into this region and no fires were burning. During the *Aqua* overpass 3 h later, slightly higher AOT was observed in this region (0.25), but corresponding cloud fraction was also higher, leading to the possibility of cloud contaminated AOT retrievals. In fact, AOT retrievals were not made along the dryline or the cold front because of the presence of clouds. Individual smoke plumes from the smaller fires are difficult to discern in the MODIS AOT product, since the MODIS AOT is only available at a 10-km resolution as compared with the 1-km resolution of the raw data.

After 1930 UTC, GOES imagery showed the increase in concentration and coverage of both the dust and smoke as the afternoon progressed (Fig. 2). The bands shown in this false color image were selected to highlight the location of dust, which is displayed by the yellow green color. These bands included GOES visible, near infrared ( $3.9 \mu\text{m}$ ), and the difference between 10.7- and  $13.3\text{-}\mu\text{m}$  data. Smoke plumes are pink, indicating that they are more sensitive to visible versus infrared radiation, but are relatively hard to discern. By 2330 UTC, the dust and smoke have become well mixed in portions of central Texas and southern Oklahoma as individual fires (pink) are no longer clearly evident, with the combined dust-smoke signature (yellow-orange) evident for distances of well over 100 km downstream of the fires. Locations of individual fires from the *GOES-12* ABBA product within  $\pm 30$  min of the image times are overlaid. The number of fire pixels increases between 1900 and 2230 UTC, corresponding to the increase in the number

and size of visible smoke plumes. By 2330 UTC, this number begins to decrease. The ABBA fire pixels are often located near the source of individual smoke plumes, though additional pixels are present that do not appear to be associated with observable smoke plumes. These pixels may represent leftover hot spots remaining after the primary fire moved on or just false detections. Another important observation is after 2130 UTC, some fire pixels were detected *under* smoke plumes originating farther west. This is especially true for the plumes in the northernmost part of Texas. One possible reason for this occurrence is the initiation of downstream fires resulting from embers lofted into the atmosphere from the initial fire. While the satellite observations support this hypothesis, they do not unequivocally prove that this is occurring. Further research into this important topic is required to better understand this link, if it exists.

Spectral signatures from multiple channels are often used to separate various features within satellite imagery such as dust and smoke aerosols from clouds and the underlying background. At midvisible wavelengths ( $0.55\ \mu\text{m}$ ) the surface reflectance values range from low (water and vegetation) to high (urban and deserts) values. At near-IR wavelengths ( $\sim 0.8\ \mu\text{m}$ ), healthy vegetation exhibits high reflectance because of chlorophyll absorption. Detecting aerosols such as smoke and dust using midvisible wavelengths over dark backgrounds is typically easier, since the reflected radiation from the aerosols is higher than the background. Over brighter backgrounds such as urban areas and deserts, these aerosols cannot be detected using midvisible wavelengths alone. The spectral signature of aerosols such as smoke and dust is generally quite different than that of clouds, but some overlap remains possible, causing misidentification. Smoke aerosols have submicrometer particle sizes and are primarily sensitive to wavelengths less than  $1.0\ \mu\text{m}$  (Reid et al. 2005). At longer wavelengths, smoke aerosols do not reflect incoming solar radiation and the satellite simply senses the underlying surface. Water clouds in the midvisible often have the same reflectance as smoke and dust aerosols, but water droplets, because of their much larger particle sizes ( $10\text{--}100\ \mu\text{m}$ ), have higher reflectance in the  $1.6\text{-}$  and  $2.1\text{-}\mu\text{m}$  channels (Greenwald and Christopher 2000). Dust plumes have particle sizes with effective diameters between  $2.0$  and  $4.0\ \mu\text{m}$  as compared with submicrometer smoke aerosols (Prospero et al. 2002), and the difference between  $11\text{-}$  and  $12\text{-}\mu\text{m}$  infrared radiation is often used to separate dust from the background regions and/or clouds (e.g., Sokolik and Toon 1999).

To compare the spectral signals of dust relative to smoke, cross sections of *Terra* and *Aqua* MODIS and *GOES-12* reflectance and brightness temperature data

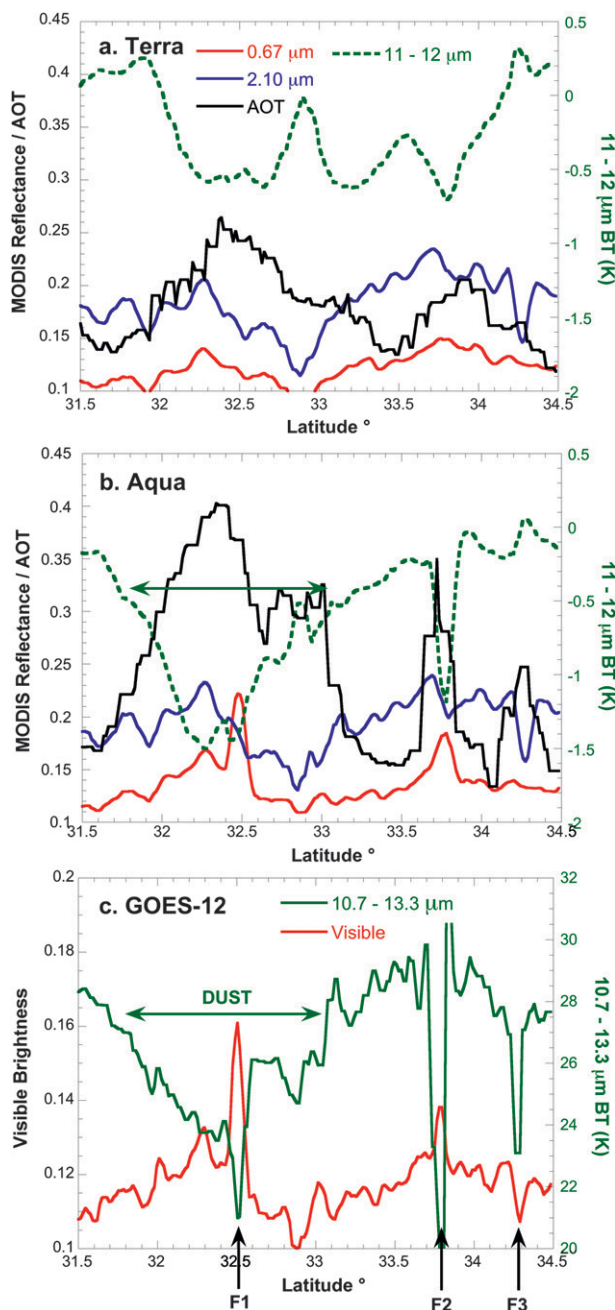


FIG. 5. Cross section of MODIS (a) *Terra* and (b) *Aqua* level 1B  $0.67\text{-}$  and  $2.1\text{-}\mu\text{m}$  reflectances and  $11\text{-}12\text{-}\mu\text{m}$  brightness temperature difference between  $31^{\circ}$  and  $34.5^{\circ}\text{N}$  at 1930 UTC. MODIS level 2 AOT at  $0.55\ \mu\text{m}$  along the same path as are the locations of the smoke plumes emanating from fires F1 and F2. (c) *GOES-12* visible reflectance and  $10.7\text{-}13.3\text{-}\mu\text{m}$  brightness temperature differences near the *Aqua* overpass time.

were analyzed from  $31.5^{\circ}$  to  $34.5^{\circ}\text{N}$  (Fig. 5). These cross sections pass through two of the largest smoke plumes ( $32.5^{\circ}$  and  $33.7^{\circ}\text{N}$ ) as well as several smaller ones in between (Fig. 1c). Reflectance at  $0.67\ \mu\text{m}$  shows a

distinct increase near the location of the smoke plumes, since they were brighter than the surface background in the visible spectrum. MODIS AOT at  $0.55\ \mu\text{m}$  also increases in proximity to the second fire with values increasing from  $<0.2$  to nearly  $0.35$  within a small  $0.3^\circ$  window. Four fires with larger smoke (and debris) plumes at the *Aqua* overpass time are labeled F1 through F4 with their origin being near Breckenridge, Texas (F1); Archer City, Texas (F2); Electra, Texas (F3); and southwest of Ardmore, Oklahoma (F4). An excellent agreement exists between the MODIS and GOES signatures at this time, with the latter also showing an increase in visible reflectance associated with the smoke plumes from F1 and F2 (Fig. 5). The smoke plume from F3 is also evident around  $34.3^\circ\text{N}$ , corresponding to another increase in AOT. However, no significant change in  $0.67\text{-}\mu\text{m}$  reflectance was observed, though a decrease in  $2.1\text{-}\mu\text{m}$  near-IR reflectance was present. In comparison with F1 and F2, the smoke plume from F3 is smaller and the source fire is farther away from the cross section. As a result, its appearance should be less apparent. The lack of a visible signal, but the presence of a near-IR signal (opposite of F1 and F2) indicates a change in aerosol properties as distance from the fire increases. (Nearer F3,  $0.67\text{-}\mu\text{m}$  reflectance does increase relative to the smoke-free background.) Along this cross section, no significant cloud cover is present; thus, changes in these reflectances are almost certainly due to aerosols. A corresponding cross section of *Terra* reflectance data was also created, and neither  $0.67\text{-}$  nor  $2.1\text{-}\mu\text{m}$  reflectance changed significantly as a function of latitude (Fig. 5a). Recall that the *Terra* overpass time was in the morning at  $\sim 1030$ ; thus, it occurred before many of the fires were spawned. The difference between *Terra* and *Aqua* reflectance emphasizes the significant growth of fires and downstream smoke plumes from the morning period into the early afternoon.

The dust storm was evident between  $31.5^\circ$  and  $33.0^\circ\text{N}$  where the brightness temperature difference between  $11\text{-}$  and  $12\text{-}\mu\text{m}$  MODIS data is negative in both *Terra* and *Aqua* data and in the  $10.7\text{--}13.3\text{-}\mu\text{m}$  difference from *GOES-12* data. The  $11\text{--}12\text{-}\mu\text{m}$  difference is much greater ( $>1.0\ \text{K}$ ) in the *Aqua* cross section compared to *Terra*, corresponding to the general increase in wind speed and dust transport over this region as the afternoon progressed (Fig. 5b). *Aqua* AOT is also maximized ( $>0.3$ ) between  $31.5^\circ$  and  $33.0^\circ\text{N}$ , corresponding to the negative  $11\text{--}12\text{-}\mu\text{m}$  values, further indicating the presence of a significant dust layer. However, this difference also becomes negative in the vicinity of the smoke plume from F2. The same signature was present in the GOES data even though  $13.3\text{-}\mu\text{m}$  data were substituted for the  $12.0\text{-}\mu\text{m}$  data. For GOES data, the differences were

positive overall, but were less positive in the vicinity of the dust plume. Visibilities remain high in the area surrounding F2; thus, widespread dust is likely not the reason for this signal. More likely, it is the larger soot and debris being lofted into the atmosphere by the fire that is causing this signal, especially since the difference quickly returns to near zero outside the smoke plume from F2. It is clear that no single visible or infrared channel is able to distinguish between the dust and smoke produced from individual fires. For example, the increase in  $0.67\text{-}\mu\text{m}$  reflectance relative to the surrounding dust is the key indicator of the location of the smoke within the larger dust plume, though soot and debris within the smoke plume itself can give a spectral signal similar to that of dust. In addition, we cannot assess the vertical extent of the dust and smoke using a single MODIS or GOES overpass.

### b. Radar data

Further quantitative assessment of the 2D and 3D characteristics of these plumes can be inferred from WSR-88D observations. It is important to emphasize again that precipitation radars are generally not sensitive to the smoke-aerosol-sized particles themselves, while they are sensitive to the large burnt debris lofted into the atmosphere and transported downstream by the prevailing winds. Since the smoke aerosols are sub-micrometer in size, it can be surmised that if debris are being detected by the radar, then large concentrations of smoke aerosols should be also be present. Dust aerosols are not associated with the fire-induced debris plumes, and since dust aerosols are also very small relative to the radar wavelength, they are generally not detectable from precipitation radar observations. A possible exception does exist near the source of the dust plume where the winds make pick up some larger debris and transport them into the atmosphere, which would be detectable from radar. However, given the lack of heat-induced buoyancy, the amount of debris is likely to be much less than that caused by wildfires.

In a complex environment that includes a dust storm and a grass fire outbreak, radars could be quickly used to distinguish dust from debris, at least given the circumstances in this example. One key factor to keep in mind is the degree to which the heights of smoke and debris are correlated near the fire source. To answer this question, we compared WSR-88D observations of debris from a forest fire in Oregon with Multiangle Imaging Spectroradiometer (MISR) Stereo Height estimates of the resulting smoke plume described by Kahn et al. (2007). The comparison between SCIT-estimated debris heights and MISR estimates of this smoke plume were  $5\ \text{km} \pm 0.5\ \text{km}$ , which we believe to be an excellent agreement.

Future research has been proposed to strengthen this connection and quantify uncertainties.

The debris plumes associated with several fires can be seen using WSR-88D reflectivity data (dBZ) combined from KDYX, KFDR, KFWS, and KTLX radars over a domain roughly 350 by 350 km<sup>2</sup> between 1900 and 2330 UTC (Fig. 3) corresponding to time of *GOES-12* images in Fig. 2. Between 1900 and 2030 UTC, the number of debris plumes and their size increase substantially behind the eastward-progressing dryline. At 1900 UTC, only F2 was producing a large debris plume, with the other fires only just beginning (Fig. 3a). The plumes from each fire appear to evolve in a unique fashion during following 6 hours. The debris plume from F1 was most evident at 1930 and 2030 UTC before dissipating thereafter though another fire appeared to start just north of F1's origin at 2330 UTC producing another debris plume (Fig. 3f). By comparison, F2 was clearly evident throughout the entire 6-h period with reflectively values in excess of 20 dBZ often present. By 2030 UTC, F2 appeared to break up somewhat into multiple debris plumes, indicating the possibility that heated debris from the original fire were sparking additional fires downstream. This is consistent with the GOES fire pixel detections, which also show hot spots downwind of some fires, but we emphasize further research is required to prove if this link exists.

Between F1 and F2 another fire intensified near Jacksboro, Texas, and by 2330 UTC the debris plumes associated with this fire and F2 extended more than 100 km downstream of the original source. Given the relatively large size of the debris ( $D > 100 \mu\text{m}$ ), they would generally be expected to fall out of the atmospheric within an hour or less, limiting their potential to be transported far downstream. In this case, winds gusting to  $30 \text{ m s}^{-1}$  easily allow a downstream transport of 100 km or more before most radar observable particles would likely fall out of the atmosphere, which is consistent with the radar observations. Farther north, the debris plumes associated with F3 and F4 were generally smaller and shorter lived. F3 was visible as a long thin debris plume at 1930 and 2030 UTC. Afterward, this fire weakens and debris associated with it was no longer detectable from radar. Fire F4 in southern Oklahoma comprises several small fires in close proximity to one another. The debris plumes associated with these fires were most evident just after passage of the dryline ( $\sim 1900$  UTC) up to 2330 UTC.

The debris plume observations from radar agree well with satellite-based smoke plume observations, indicating that both are collocated much of the time. Using this assumption, radar data can be used to estimate the height to which debris (and by extrapolation smoke aerosols) is lofted into the atmosphere. A cross section of radar data

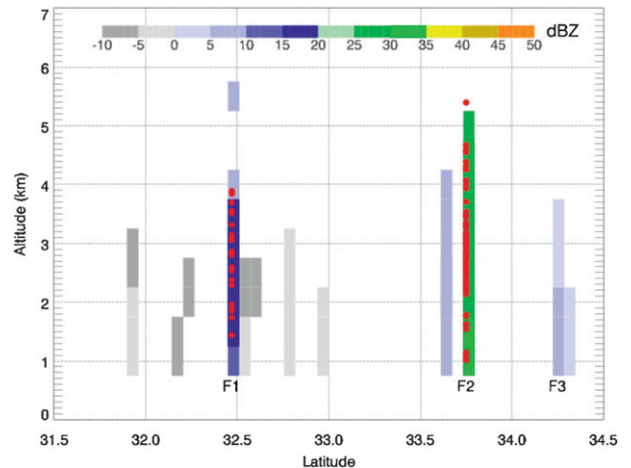


FIG. 6. Cross section of radar reflectivity data at 1930 UTC from (left to right plots) KDYX, KFDR, KFWS, and KTLX between 31° and 34.5°N with corresponding locations of three debris plumes originating from F1, F2, and F3. Red dots indicate the debris plume detections from SCIT associated with each fire as a function of derived maximum injection height for each detection.

through the stronger debris plumes, located along the same path as the satellite cross section, shows that the grass and other burnt debris were reaching at least 5 km into the atmosphere (Fig. 6). Maximum reflectivity values were again associated with F2 with reflectivity greater than 20 dBZ being observed at 5 km. The locations of the debris plumes based on radar data correspond almost exactly to the locations of high MODIS visible reflectance values calculated along the same path (Fig. 5b), emphasizing the close relationships between debris-sized particles and smoke aerosols. As before, the reflectivity returns associated with F3 are both weaker and not as high in the atmosphere compared to F1 and F2.

Plume heights generated from modified severe storm algorithms provide a unique insight into the evolution of individual debris plumes and the height to which debris are being lofted into the atmosphere. Detections associated with the major fires are shown in Fig. 3 along with the raw radar data. F1 was visible from the KDYX and KFWS radars, though all but two of these detections were from KDYX (Fig. 7a). Detections from KDYX began to be generated shortly after 1800 UTC, with many “storm cell” heights between 1 and 3.5 km derived from SCIT (Fig. 7). However, the injection heights decreased after 2100 UTC, only reaching 2 km, consistent with the 2D radar observations in Fig. 3. By 0000 UTC 10 April, the fire was no longer detectable using the modified SCIT algorithm, though it does remain evident within the raw radar data for a few more hours. Debris plume heights associated with F2 do not decrease as fast as F1 and heights from KFDR are consistently in the

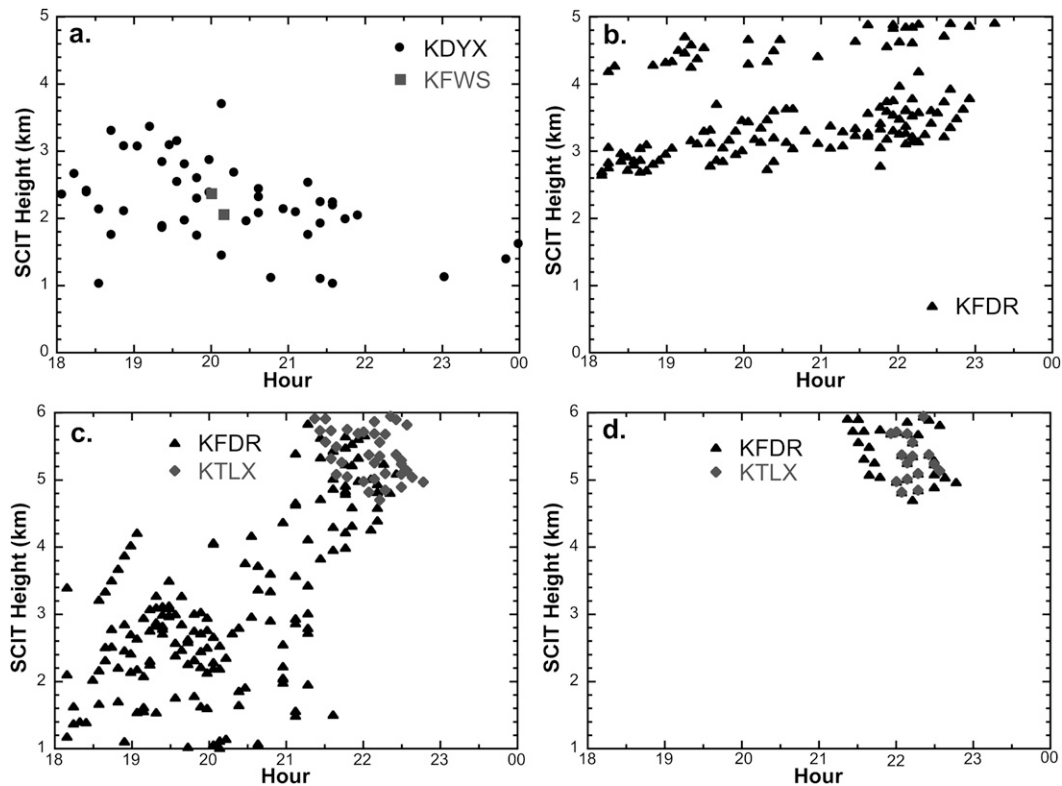


FIG. 7. SCIT storm cell heights associated with fires (a) F1, (b) F2, (c) F3, and (d) F4 between 1800 UTC 9 Apr and 0000 UTC 10 Apr. Both F3 and F4 occurred within detection range of KFDR and KTLX providing height information from two different perspectives for these fires.

4–5-km range, with no decrease in heights observed until after 0000 UTC (Fig. 7b). MODIS data support the radar observations, as F2 appeared to have the largest plume of all those observed near the *Aqua* overpass time of 1930 UTC. Moving on to F3 and F4, injection heights of 4–5 km were also observed (Figs. 7c,d). Despite the comparatively small plume, detections associated with F3 ranged between 1 and 3.5 km between 1700 and 1900 UTC with height gradually increasing with time. As the fire and debris plume progressed eastward, it came within range of KTLX, producing multiple detections above 4 km between 1900 and 2000 UTC. F4 was the northernmost of the four fires examined in detail and heights of over 4 km were estimated from both KFDR and KTLX radar data. Since smoke aerosol particles are smaller and lighter, they were likely being transported even higher into the atmosphere than the modified severe storm algorithm is reporting. This information concerning the injection height from can be vital to accurate modeling of downstream aerosol and air quality conditions, since current remote products from MISR and Cloud–Aerosol Lidar and Infrared Pathfinder Satellite Observations (CALIPSO) have many limitations.

## 5. Summary and future applications

Using the multiple remote sensing platforms, we were able to assess smoke and debris plume properties from the 9 April 2009 grass fires in great detail. Multispectral observations from the satellite data proved quite useful in detecting the locations of both dust and smoke plumes and discriminating between the two different aerosol types. Visible spectrum reflectance was able to distinguish smoke plumes from the surface background while infrared spectrum data were useful in detecting smoke plumes and separating smaller smoke signatures within the larger dust plume. The MODIS AOT product adequately sampled the location of the dust aerosols but often failed to capture aerosol concentrations associated with individual smoke plumes because of comparatively poor spatial resolution of the aerosol product ( $10 \text{ km}^2$ ). GOES data showed similar features as MODIS but at a much higher temporal resolution, allowing for the examination of dust and smoke plume evolution throughout the event. These data indicated a general increase in the areal coverage of both dust and smoke between 1900 and 2300 UTC with both aerosol types becoming mixed as they were being advected downwind. The GOES ABBA

fire product also showed an increase in the number of detected fires during this period, only decreasing after 2300 UTC.

Precipitation radars were unable to sample aerosols associated with the dust storm but did sample debris plumes associated with the individual fires at both high spatial and temporal resolutions. Using the radar data, we assessed the temporal evolution of debris plumes using radar reflectivity returns from burnt debris lofted into the atmosphere. The location of these plumes corresponded well with available satellite observations of the initiation location and spatial extent of downstream smoke plumes. The temporal and spatial extents of the debris and smoke plumes from independent radar and satellite observations were quite similar, but each provides unique information not available from the other further emphasizing the advantages of a multisensor approach. Radar data were also useful at determining the height to which debris were being injected into the atmosphere, which was greater than 5 km for the largest debris plumes (F1 and F2). Smoke and debris remained suspended in the atmosphere for hours affecting conditions over 100 km downwind of the fires themselves.

Currently, no objective system exists that uses all these data sources in near-term fire weather and/or air quality forecasts. In terms of air quality modeling, the 3D information of the debris plume can be incorporated into the initialization process to improve overall air quality forecasts. Many current air quality models rely on either satellite observations or sparse surface networks, which are not capable of providing the complete picture of the amount of smoke and debris being lofted into the atmosphere. This research represents a first step at quantifying debris plume properties from radars, but additional research and validation is necessary. Most importantly, a quantitative link between debris properties observed from radars and smoke properties observed from satellites (and used as inputs to air quality models) must be derived. Preliminary comparisons with MISR Stereo Height data do show an excellent agreement in injection height values, and further research is under way to estimate uncertainties.

Further improvements in radar debris plume algorithms and derived properties will also be important. This leads into another important application of this research—fire weather analysis and forecasting. Radar data can be used to determine the approximate location of individual fires where the maximum amount of debris is being injected into the atmosphere and the propagation speed of these features. These observations could be very important to those downstream of a fire, by allowing for an estimate of the time and significance of its impacts to be made. These methods would be extremely useful when ground-based

observations are not possible because of either poor conditions or remoteness of the fire. The use of radar data and algorithms designed to detect debris plume properties allows for this information to be available in near-real time, which is a very important consideration.

The research also indicates the possibility that lofted embers falling out of a debris plume may be sparking fire downwind of the original fires. While this is not proved by this research, such a possibility cannot be ignored and will be explored in the future. Finally, multi-radar analysis of debris plumes using Doppler radars allows for the retrieval of the 3D wind data within the plume. This information could be compared with ground observations to improve the understanding of fire dynamics as well as integrated into air quality and/or debris dispersion models. We strongly believe inclusion of such data into such tools will be extremely advantageous in future forecasting of fire related impacts.

*Acknowledgments.* This work is supported by NOAA Air Quality grants at the University of Alabama in Huntsville. The MODIS data were acquired through the level 1 and Atmosphere Archive and Distribution System and GOES ABBA data from the NRL FLAMBE project. WSR-88D level 2 data were acquired from the NCDC archive using the HDSS Access System.

#### REFERENCES

- Banta, R. M., L. D. Olivier, E. T. Holloway, R. A. Kropfli, B. W. Bartram, R. E. Cupp, and M. J. Post, 1992: Smoke-column observations from two forest fires using Doppler lidar and Doppler radar. *J. Appl. Meteor.*, **31**, 1328–1349.
- Cheney, N. P., and J. S. Gould, 1995: Fire growth in grassland fuels. *Int. J. Wildland Fire*, **5**, 237–247.
- Christopher, S. A., P. Gupta, U. Nair, T. A. Jones, S. Kondragunta, Y. Wu, J. Hand, and X. Zhang, 2009: Satellite remote sensing and mesoscale modeling of the 2007 Florida/Georgia fires. *IEEE J. Select. Topics Appl. Earth Sci. Remote Sens.*, **26**, 1–13.
- Chu, D. A., Y. J. Kaufman, C. Ichoku, L. A. Remer, D. Tanré, and B. N. Holben, 2002: Validation of MODIS aerosol optical depth retrieval over land. *Geophys. Res. Lett.*, **29**, 8007, doi:10.1029/2001GL013205.
- Clark, T. L., L. F. Radke, J. L. Coen, and D. Middleton, 1999: Analysis of small-scale convective dynamics in a crown fire using infrared video camera imagery. *J. Appl. Meteor.*, **38**, 1401–1420.
- Clements, C. B., and Coauthors, 2007: Observing the dynamics of wildland grass fires: FireFlux—A field validation experiment. *Bull. Amer. Meteor. Soc.*, **88**, 1369–1382.
- Coen, J., S. Mahalingam, and J. Daily, 2004: Infrared imagery of crown-fire dynamics during FROSTFIRE. *J. Appl. Meteor.*, **43**, 1241–1259.
- Crum, T. D., and R. L. Albery, 1993: The WSR-88D and the WSR-88D Operational Support Facility. *Bull. Amer. Meteor. Soc.*, **74**, 1669–1687.

- Giglio, L., J. D. Kendall, and R. Mack, 2003: A multi-year active fire data set for the tropics derived from the TRMM VIRS. *Int. J. Remote Sens.*, **24**, 4505–4525.
- Greenwald, T. J., and S. A. Christopher, 2000: The GOES-IM imagers: New tools for studying the microphysical properties of boundary layers clouds. *Bull. Amer. Meteor. Soc.*, **81**, 2607–2620.
- Johnson, J. T., P. L. MacKeen, A. Witt, D. Mitchell, G. J. Stumpf, M. D. Eilts, and K. W. Thomas, 1998: The storm cell identification and tracking algorithm: An enhanced WSR-88D algorithm. *Wea. Forecasting*, **13**, 263–276.
- Jones, T. A., and S. A. Christopher, 2009: Injection heights of biomass burning debris estimated from WSR-88D radar observations. *IEEE Trans. Geosci. Remote Sens.*, **47**, 2599–2605.
- , and —, 2010: Satellite and radar observations of the 9 April 2009 Texas and Oklahoma grassfires. *Bull. Amer. Meteor. Soc.*, **91**, 455–460.
- , —, and W. Petersen, 2009: Dual-polarimetric radar characteristics of an apartment fire. *J. Atmos. Oceanic Technol.*, **26**, 2257–2269.
- Justice, C. O., and Coauthors, 2002: The MODIS fire products. *Remote Sens. Environ.*, **83**, 244–262.
- Kahn, R. A., W. H. Li, C. Moroney, D. J. Diner, J. V. Martonchik, and E. Fishbein, 2007: Aerosol source plume physical characteristics from space-based multiangle imaging. *J. Geophys. Res.*, **112**, D05S17, doi:10.1029/2006JD007647.
- Levy, R. C., L. A. Remer, S. Mattoo, E. F. Vermote, and Y. J. Kaufman, 2007: Second-generation operational algorithm: Retrieval of aerosol properties over land from inversion of Moderate Resolution Imaging Spectroradiometer spectral reflectance. *J. Geophys. Res.*, **112**, D13211, doi:10.1029/2006JD007811.
- Melnikov, V. M., D. S. Zurnic, R. M. Rabin, and P. Zhang, 2008: Radar polarimetric signatures of fire plumes in Oklahoma. *Geophys. Res. Lett.*, **35**, L14815, doi:10.1029/2008GL034311.
- National Weather Service, cited 2009: Norman Oklahoma, 2009, Event summary for the wildfire outbreak of April 9th 2009. [Available online at <http://www.srh.noaa.gov/oun/?n=events-20090409>.]
- Prados, A. I., S. Kondragunta, P. Ciren, and K. R. Knapp, 2007: GOES Aerosol/Smoke Product (GASP) over North America: Comparisons to AERONET and MODIS observations. *J. Geophys. Res.*, **112**, D15201, doi:10.1029/2006JD007968.
- Prins, E. M., and W. P. Menzel, 1994: Trends in South American biomass burning detected with the GOES visible infrared spin scan radiometer atmospheric sounder from 1983 to 1991. *J. Geophys. Res.*, **99**, 16 719–16 735.
- Prospero, J. M., P. Ginoux, O. Torres, S. Nicholson, and T. E. Gill, 2002: Environmental characterization of global sources of atmospheric soil dust derived from NIMBUS 7 Total Ozone Mapping Spectrometer (TOMS) absorbing aerosol product. *Rev. Geophys.*, **40**, 1002, doi:10.1029/2000RG000095.
- Reid, J. S., and Coauthors, 2005: A review of biomass burning emissions. Part III: intensive optical properties of biomass burning particles. *Atmos. Chem. Phys.*, **5**, 827–849.
- Remer, A., and Coauthors, 2005: The MODIS aerosol algorithm, products, and validation. *J. Atmos. Sci.*, **62**, 947–973.
- Rogers, R. R., and W. O. Brown, 1997: Radar observations of a major industrial fire. *Bull. Amer. Meteor. Soc.*, **78**, 803–814.
- Rothermel, R. C., 1991: Predicting behavior and size of crown fires in the northern Rocky Mountains. U.S. Dept. of Agriculture, Forest Service, Intermountain Research Station, Research Paper INT-438, 46 pp.
- Sokolik, I., and O. Toon, 1999: Incorporation of mineralogical composition into models of the radiative properties of mineral aerosol from UV to IR wavelengths. *J. Geophys. Res.*, **104** (D8), 9423–9444.
- Weaver, T., 2006: A word to the firewise. *Wildland Firefighter*, **10**, 25–30.
- Wilhite, D. A., K. H. Smith, and M. J. Hayes, 1996: The National Drought Mitigation Center. *Proc. Conserv '96*, Washington, DC, American Water Works Association, 795–799.